

Oxygen-induced near-surface structural rearrangements on Ni{001} studied by shadow-cone-enhanced secondary-ion mass spectrometry

C. Xu, J. S. Burnham, S. H. Goss, K. Caffey, and N. Winograd

Department of Chemistry, The Pennsylvania State University, 152 Davey Laboratory, University Park, Pennsylvania 16802

(Received 22 July 1993)

The surface structure of Ni{001} and the adsorption systems $p(2\times 2)$ O/Ni{001} and $c(2\times 2)$ O/Ni{001} have been studied by shadow-cone-enhanced secondary-ion mass spectrometry. The secondary Ni⁺-ion intensity has been measured as a function of the incidence angle of the primary Ar⁺-ion beam. The enhanced intensity features in the spectra are compared with results from a two-body-interaction calculation which uses the Molière approximation to the Thomas-Fermi potential. For the clean Ni{001} surface the analysis indicates that the spacing between the first and second layer decreases from the bulk value of 1.76 to 1.68 ± 0.06 Å. Moreover, the spacing between the second layers and the third layer remains nearly bulklike at 1.74 ± 0.16 Å. For the oxygenated surfaces the O-Ni bond length is determined to be 1.96 ± 0.05 Å, which corresponds to a height for the oxygen of 0.85 Å above the Ni substrate. The presence of oxygen is found to cause buckling in the second Ni layer in accord with previous low-energy-electron-diffraction observations. The magnitude of the buckling is found to be 0.26 ± 0.12 Å and 0.20 ± 0.10 Å for the $p(2\times 2)$ and $c(2\times 2)$ surfaces, respectively. These results suggest that the O-Ni bonding is highly localized and only modestly dependent upon coverage.

I. INTRODUCTION

Oxygen adsorption on Ni{001} is a model for studying the oxidation of a metal surface. Numerous techniques such as low-energy electron diffraction (LEED),¹⁻⁷ surface extended x-ray-absorption fine structure (EXAFS),^{8,9} He scattering,^{10,11} high-resolution electron-loss spectroscopy (HRELS),¹²⁻¹⁵ and Rutherford backscattering (RBS) (Refs. 16 and 17) have been brought to bear on this system. From these studies, it is generally accepted that oxygen adsorbs in the fourfold hollow site for both the $p(2\times 2)$ (0.25 monolayer oxygen coverage) and the $c(2\times 2)$ (up to 0.5 monolayer coverage) structures. Most of these studies also show that the oxygen atom is adsorbed about 0.9 Å above the Ni surface for both coverages. The exact nature in which the substrate surface relaxes and reconstructs due to the presence of an oxygen overlayer is still controversial. Investigations carried out by RBS (Refs. 16 and 17) have indicated that the outermost Ni layer is relaxed inward before oxygen adsorption (relative to the bulk interlayer spacing), and is expanded after oxygen adsorption, but many other studies mentioned above have assumed a bulklike structure in their analysis. Furthermore, results from a recent LEED investigation^{18,19} suggest that the $p(2\times 2)$ and $c(2\times 2)$ surfaces form a buckled layer below the surface.

Here we report an investigation of the structure of the clean Ni{001}, $p(2\times 2)$ O/Ni{001}, and $c(2\times 2)$ O/Ni{001} surfaces with shadow-cone-enhanced secondary-ion mass spectrometry (SIMS). With this method, the collision of a keV projectile with a surface atom creates a shadow cone, which focuses the incident flux to specific coordinates. This flux is sharply peaked at the shadow-cone edge and exhibits a width of less than 0.02 Å.²⁰ When the tail of this shadow cone strikes a surface or near-surface atom, the atomic motion near the

surface should dramatically increase, resulting in an enhancement of the ejection yield. In contrast, if the shadow-cone edge falls between atoms, the surface motion and resulting yield are low. In effect, we can "aim" the incident beam to specific high-action points on the target. With knowledge of the shadow-cone shape, it is then feasible to determine specific geometries using simple triangulation. For certain geometries, it is possible to obtain information from the first several layers of the crystal. This technique has been applied to the characterization of metal,²¹ semiconductor,²² and adatom/metal²³ surfaces. The collision and ejection mechanisms, which yield the structural information, have been verified by a three-dimensional molecular-dynamics simulation.²⁴ With this result as a basis, a computationally less-intensive approach has also been developed in which the shadow-cone shape is calculated from a two-body collision model employing a Thomas-Fermi potential.²⁴ This approach to surface-structure elucidation offers the advantage that the bond lengths can be directly derived from the data. They do not depend upon a fitting procedure which selects a bond length from a set of trial structures that yield the least overall error.

Our results show that the Ni lattice undergoes systematic rearrangements in response to the new electronic environment associated with chemisorbed oxygen atoms. For instance, the first interlayer spacing of the clean surface is determined to be 1.68 ± 0.06 Å, which is contracted from the bulk spacing of 1.76 Å. The second interlayer spacing, however, remains almost bulklike. Oxygen adsorption on the surface induces rearrangements, which are found to be coverage dependent. The oxygen atom adsorbs in a fourfold hollow site and for both the $p(2\times 2)$ and $c(2\times 2)$ structures is found to bind 0.85 ± 0.11 Å above the top Ni plane. In both structures, the second-layer Ni atom, which is located directly beneath an oxy-

gen atom is pushed lower than other atoms in the same plane. Therefore, the second layer is buckled where the amplitude is $0.26 \pm 0.12 \text{ \AA}$ for the $p(2 \times 2)$ layer and $0.20 \pm 0.12 \text{ \AA}$ for the $c(2 \times 2)$ layer. These results generally support earlier LEED studies^{18,19} and suggest that the oxygen bonding is localized for both coverages. The shadow-cone measurements also allow other structural rearrangements, which occur during oxygen chemisorption, to be closely monitored. Due to the buckling, the values for the interlayer spacing may be referred to a weighted average of the second-layer atom positions. Referenced in this way, the first interlayer spacing expands upon oxygen adsorption to $1.72 \pm 0.06 \text{ \AA}$ for the $p(2 \times 2)$ structure and to $1.88 \pm 0.06 \text{ \AA}$ for the $c(2 \times 2)$. The second interlayer spacing is found to contract slightly in tandem with this expansion, the value changing from $1.70 \pm 0.16 \text{ \AA}$ for the $p(2 \times 2)$ to $1.61 \pm 0.16 \text{ \AA}$ for the $c(2 \times 2)$ structure.

II. EXPERIMENTAL ASPECTS

The experimental apparatus employed in this study has been described elsewhere.^{25–27} Only a few specific aspects will be detailed here. The configuration of the setup is shown schematically in Fig. 1. The polar angle of incidence θ_i is defined with respect to the surface normal. The angle β is defined as the angle between the incident ion beam and the detector and the angle θ_d defines the angle between the detector and the surface normal. In this study, the Ni sample is aligned such that either the $\langle 100 \rangle$ or $\langle 110 \rangle$ direction is parallel to the plane defined by the detector and incident ion beam. The desorbed secondary-ion intensity is then measured as a function of mass and θ_i of the projectile, while β is fixed at 16° . Note that either the forward edge or the backward edge of the shadow cone may intersect surface or near-surface atoms. These edges are designated in Fig. 1. The mass analyzer is currently only capable of measuring positive ion signals. An energy prefilter is used to select those ions with kinetic energies equal to $13 \pm 0.2 \text{ eV}$.

The Ni{001} crystal is a 1.3-cm-diam disk oriented to

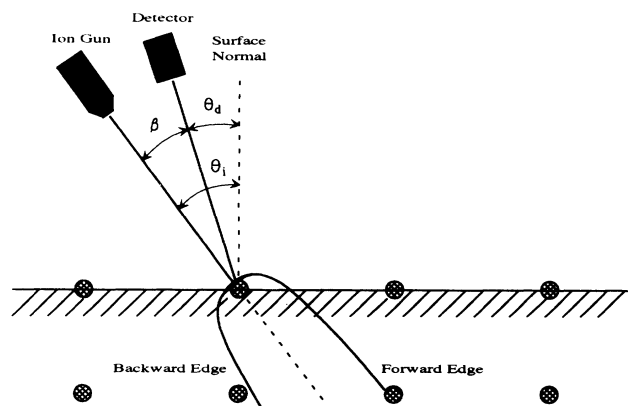


FIG. 1. Definition of the angles used in shadow-cone-enhanced SIMS experiments. A schematic of the shadow cone is illustrated with the forward and back edge designated as shown.

within $\pm 0.5^\circ$ and commercially polished. The sample preparation includes *in situ* cycles of annealing at 1050 K and 3-keV Ar^+ bombardment ($1 \mu\text{A}$ with a 1.5-cm-diam spot). The presence of surface contaminants was monitored by SIMS and LEED. In the experiment, the incident 3-keV Ar^+ -ion beam was typically operated at a current of 10–20 nA with a 2-mm-diam spot size. The sample was stepped in the vertical axis over a 10-mm range for every measurement in order to reduce the amount of ion-beam-induced surface damage. For the oxygen overlayer experiments, the oxygen (99.99%) was introduced into the chamber from a gas inlet system by a variable leak valve. The sample was positioned directly in front of the leaking port and the sample temperature was maintained at 300 K during dosing. Ordered $p(2 \times 2)$ and $c(2 \times 2)$ overlayers were prepared by dosing with an uncalibrated oxygen dose sufficient to obtain the appropriate LEED pattern. The $p(2 \times 2)$ structures were annealed for 5 min at 450 K and the $c(2 \times 2)$ structures were annealed for 15 min at 450 K. The shadow-cone experiments were then performed at 300 K.

III. RESULTS AND DISCUSSION

A. The clean Ni{001} surface

A schematic of the top view of the Ni{001} surface is shown in Fig. 2. The side views along the $\langle 100 \rangle$ and $\langle 110 \rangle$ azimuths are shown in Fig. 3. The atoms that are most likely to be involved in shadow-cone interactions are designated by their positions in columns and rows. These labels are shown in Fig. 3. In our nomenclature, a collision of the primary ion with atom (1,1) followed by the intersection of the forward edge of the shadow cone with atom (1,3) would be designated $F(1,1)(1,3)$. An intersection involving the backward edge of the shadow cone would be labeled $B(1,1)(1,3)$. Similar notation is used to describe mechanisms involving shadow cones produced by oxygen atoms. For these cases, the adsorbate layer is designated by (Ox), and a typical interaction would be

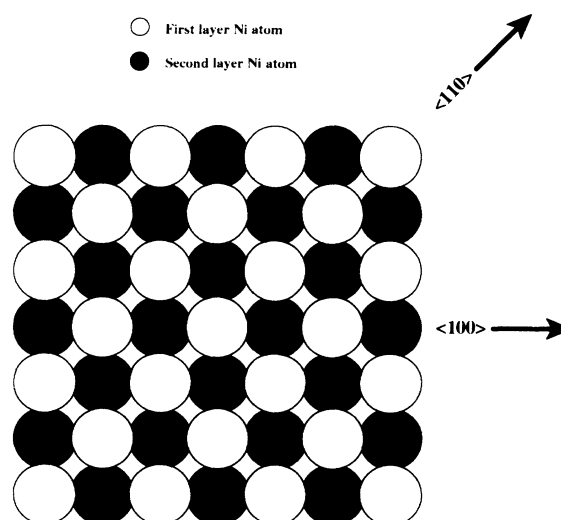


FIG. 2. A schematic of the Ni{001} model surface.

$B(Ox)(2,4)$. The radius of a shadow cone created by 3-keV Ar^+ -Ni interactions is less than 1.70 Å at a distance of 10 Å along the shadow cone. For the $\langle 100 \rangle$ azimuth, the interplanar spacing is about 1.76 Å, so the analysis can be specific to interactions of in-plane atoms. For the $\langle 110 \rangle$ azimuth, the interplanar spacing is about 1.25 Å so it is necessary to consider scattering from atoms that are out of plane.

The desorbed secondary Ni^+ -ion intensities as a function of the ion-beam incidence angle measured in the $\langle 100 \rangle$ and the $\langle 110 \rangle$ azimuths are shown in Figs. 4 and 5. In the spectra, $\theta_i = 0^\circ$ refers to bombardment normal to the surface, and $\theta_i = 90^\circ$ refers to bombardment parallel to the surface. Generally, spectra for each azimuth are characterized by a broad intensity enhancement at high polar angles and a sharp peak at $\theta_i = 22.6^\circ$. For the incidence angle distribution along the $\langle 100 \rangle$ azimuth, there is a valley at $\theta_i = 45^\circ$, while for the $\langle 110 \rangle$ azimuth, the valley appears in the spectrum at $\theta_i = 35^\circ$. These two angles are in excellent agreement with the $\langle 101 \rangle$ and $\langle 112 \rangle$ crystallographic indexes, respectively. At these

incident angles, the shadow cone created by the interaction of a surface atom with the incident ion beam channels the projectiles deep into the solid. The channeling of the ion beam reduces the interactions of incident ions with surface atoms, which decreases the desorption of secondary ions.

In order to relate the intensity enhancements in the spectra to the surface structure, it is necessary to determine the shadow-cone shape of the incidence/surface-atom interactions. The 3-keV Ar^+ /Ni interaction is described by a two-body collision model, which uses the Molière approximation to a Thomas-Fermi potential. This potential function requires knowledge of the Firsov screening factor for a given pair of colliding atoms with atomic number Z_1 for the projectile and Z_2 for the target. This factor f may either be determined using an empirical relation²⁸ of the form

$$f(Z_1, Z_2) = 0.54 + 0.045[(Z_1)^{1/2} + (Z_2)^{1/2}] \quad (1)$$

or by direct experimental measurement using a system

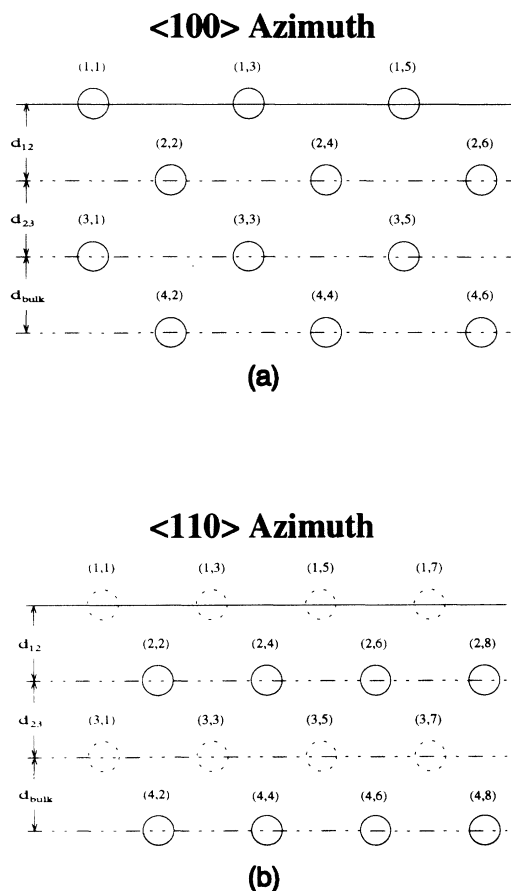


FIG. 3. Cross sections of the $Ni\{001\}$ surface indicating the atomic plane geometry parallel to (a) the $\langle 100 \rangle$ crystal direction and (b) the $\langle 110 \rangle$ crystal direction. The atoms are designated by their positions in rows and columns. The dotted circles represent atoms that are out of plane. Note that the degeneracy between mechanism (1,1)(2,4) and (1,3)(2,6) is removed by the presence of an adsorbed oxygen atom.

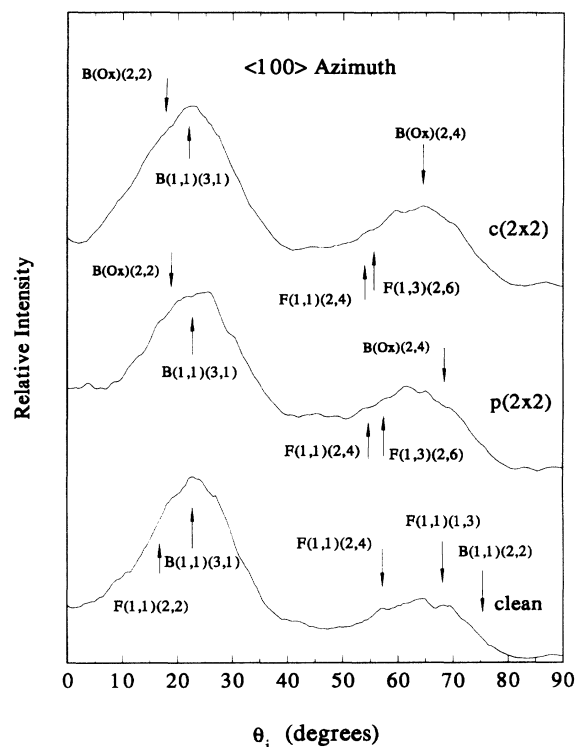


FIG. 4. The relative intensity of 13-eV Ni^+ ions desorbed from clean $Ni\{001\}$, $p(2 \times 2)$ $O/Ni\{001\}$, and $c(2 \times 2)$ $O/Ni\{001\}$ plotted as a function of the ion-beam incident angle. The ion beam is parallel to the $\langle 100 \rangle$ crystal direction. The arrows indicate the position of angles calculated from results of a two-body collision model for the optimized, relaxed model described in the text. The capital letters F and B designate the forward and back edges of the shadow cone, respectively. The coordinates of the atom creating the shadow cone are followed by the coordinates of the atom on which the ion beam is being focused. The error bars are shown in Fig. 6. See text for more details.

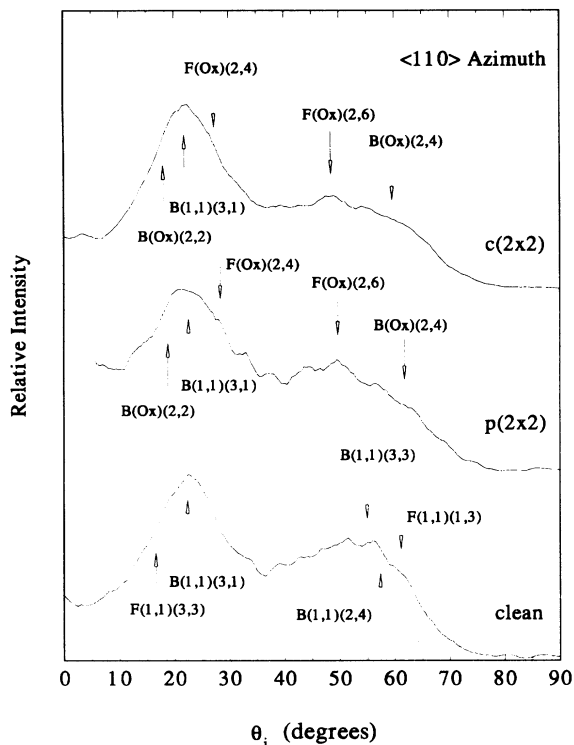


FIG. 5. The relative intensity of 13-eV Ni^+ ions desorbed from clean $\text{Ni}\{001\}$, $p(2 \times 2)$ $\text{O}/\text{Ni}\{001\}$, and $c(2 \times 2)$ $\text{O}/\text{Ni}\{001\}$ plotted as a function of the ion-beam incident angle. The ion beam is parallel to the $\langle 110 \rangle$ crystal direction. The error bars are the same as in Fig. 6. See caption to Fig. 4 for more details.

with known bond lengths. From Eq. (1), using $Z_1 = 18$ for Ar and $Z_2 = 28$ for Ni, $f(Z_1, Z_2) = 0.97$.

The experimental calibration of $f(Z_1, Z_2)$ can be evaluated using the $F(1,1)(1,3)$ interaction along the $\langle 100 \rangle$ azimuth. This feature results from an ejection mechanism whereby the incident ions are deflected by a first-layer atom and collide with the nearest atom of the same layer along the incident direction. For this distance, LEED and RBS measurements²⁹⁻³³ indicate that there is no significant lateral displacement in the surface atomic layer of $\text{Ni}\{001\}$. Using the known bulk spacing of 3.52 Å, we then calculate a Firsov screening factor of 1.00 ± 0.01 , a value in good agreement with that calculated from Eq. (1).

After the shadow-cone shape is determined, the surface-structure analysis is performed in two steps. In the first step, the incidence angles at which a shadow cone interacts with neighboring atoms are calculated for a given surface-structure model. In the second step, the calculated results are compared with the enhanced intensity features in the experimental angular distributions. The surface-structure model is then adjusted to improve the fit between the calculated and experimental data.

The calculated angles associated with possible interaction mechanisms involving the first few layers are shown in Table I. From these values, it is possible to assign many of the features observable in the experimental

TABLE I. Calculated and measured shadow-cone intersection mechanisms for clean $\text{Ni}\{001\}$

Azimuth	Mechanism	Calculated		Calculated, Relaxed ^c
		Bulk ^a	Measured ^b	
$\langle 100 \rangle$	$F(1,1)(2,2)$	16.3		17.2
	$B(1,1)(3,1)$	22.1	22.6	22.6
	$F(1,1)(2,4)$	56.1	56.8	56.8
	$F(1,1)(1,3)$	67.9	68.1	68.1
	$B(1,1)(2,2)$	73.7		75.5
$\langle 110 \rangle$	$F(1,1)(3,3)$	16.5		16.9
	$B(1,1)(3,1)$	22.1	22.6	22.6
	$F(1,1)(3,5)$	40.5		41.1
	$B(1,1)(4,4)$	43.3		43.8
	$B(1,1)(3,3)$	54.2		55.2
	$B(1,1)(2,4)$	56.2		57.2
	$F(1,1)(1,3)$	61.3		61.3

^aCalculated values of θ_i in degrees associated with shadow-cone-enhanced intensity features assuming bulk bond distances.

^bMeasured values of θ_i in degrees associated with intensity maxima. No value indicates that the expected feature is not sharp enough to characterize accurately.

^cCorresponding values of θ_i in degree reported for the relaxed structure which best fits the measured data.

curves reported in Figs. 4 and 5. These correlations are also noted in Table I. Finally, the bond distances in the surface layers can be adjusted so that the best global fit can be obtained between the calculated and measured features. The angles of the shadow-cone mechanisms associated with the relaxed surface are shown in Table I and in Figs. 4 and 5.

Several of the features are particularly well defined. The $B(1,1)(3,1)$ enhanced intensity feature, which occurs at an incidence angle of 22.6° , is pronounced for both azimuths. The mechanism causing the enhanced intensity involves incident ions that are deflected by the first-layer atom in position (1,1) and focused onto the coordinates (3,1) in the third layer directly below. When the focused flux impinges on this atom, the momentum transfer is maximized and the number of desorbed ions is observed to increase. The spacing between the first and third atomic layers is determined from this feature to be 3.42 ± 0.10 Å, a value slightly smaller than the bulk spacing of 3.52 Å. In the $\langle 100 \rangle$ azimuth, the enhanced intensity feature $F(1,1)(2,4)$ at $\theta_i = 56.8^\circ$ can be used to determine the first interlayer spacing. The spacing, calculated to be 1.68 ± 0.06 Å, indicates an inward relaxation from the bulk distance of 1.76 Å. From $B(1,1)(3,1)$ and $F(1,1)(2,4)$, the interlayer spacing between the second and third layer is found to be 1.74 ± 0.16 Å, statistically equivalent to the bulk value. The top-layer relaxation structure discussed above for clean $\text{Ni}\{001\}$ is consistent with earlier RBS (Refs. 16 and 17) studies. In those experiments, the first interlayer spacing was determined to be contracted by 0.06 ± 0.01 Å, which corresponds to a spacing of 1.70 Å.

There are several other features that are not easily observed, most notably $F(1,1)(2,2)$ and $B(1,1)(2,2)$. Similar mechanisms in the $\langle 110 \rangle$ azimuth include $F(1,1)(3,3)$,

$F(1,1)(1,3)$, $B(1,1)(3,3)$, and $B(1,1)(2,4)$. These interactions are short ranged occurring in the top two layers and are expected to create a significant intensity enhancement. Since they are not pronounced other factors such as peak overlap must be present, which affect the appearance of intensity enhancements. For example, the $F(1,1)(3,3)$ mechanism in the $\langle 110 \rangle$ azimuth overlaps with the feature $B(1,1)(3,1)$ and appears as a slight shoulder on the overall peak. A second example includes the $B(1,1)(3,3)$ and $B(1,1)(2,4)$ mechanisms, which are so close that they appear as one feature. Current work is focused on obtaining a clearer understanding of these processes so that it might be possible to construct methods which may resolve some of these complexities. Since these features are either overlapping with other bands or are not very strong, we have chosen not to attempt to utilize these mechanisms in structure determinations. For these reasons we have not included these features in Table I.

At this stage, it is useful to discuss the relative accuracy and precision of these measurements. There are at least four aspects to this issue. First, there are possible systematic errors associated with distortions of the shadow cone due to the presence of neighboring atoms. The effect of these distortions has been discussed previously.²¹ It is important to avoid geometrical configurations where these distortions can be a problem. Ideally, it is better to have more than one set of mechanisms, which can be used as an internal check of the assignments, although this is not always possible. It is also desirable to verify that distortions are not a problem by changing the incident energy or incident-ion mass. The second issue involves the fact that the theory is assumed to apply for emitted neutral species and the experimental apparatus detects secondary ions formed in the collision process. For values of θ_d between $\pm 45^\circ$, this difference is very small since image charge effects and reneutralization have been shown to have a negligible influence on measured peak angles.²¹ A third issue is the experimental reproducibility of peak position assignments. The Ni^+ secondary-ion distributions shown in Figs. 4 and 5 are the sum of several individual spectra that were obtained over a time period of a few months. In each of the individual spectra, the features used in this analysis are reproducible within $\pm 0.5^\circ$, which translates into an uncertainty of less than $\pm 0.06 \text{ \AA}$ in most cases. Finally, there is the issue of overlapping peaks. As noted above, there are several features that are observable between $\theta_i = 56^\circ$ and 77° . From examination of Fig. 3, it is clear that there is more than one possible mechanism that can contribute to intensity in this angle range. Some of the more obvious ones are summarized in Table I. Deconvolution of these features is always a risky venture, and we have not attempted to systematically resolve all of the peaks. Peak assignments, therefore, have an added uncertainty associated with these overlaps. The reported error limits include our best estimates of the influence of all of the above factors.

B. $p(2 \times 2)$ O/Ni{001} surface

The desorbed secondary Ni^+ -ion intensities as a function of the incidence angle for the $\langle 100 \rangle$ and $\langle 110 \rangle$ az-

imuths of the $p(2 \times 2)$ O/Ni{001} surface are shown in Figs. 4 and 5, respectively. The main peak in both spectra arises from the $B(1,1)(3,1)$ mechanism at $\theta_i = 22.6^\circ$, and is very similar to that found on the clean surface. The spacing between the first and third Ni layers is determined to be $3.42 \pm 0.10 \text{ \AA}$ from this feature, in excellent agreement with what was found on the clean surface. Along the $\langle 100 \rangle$ azimuth (Fig. 4), there are two enhanced intensity features, $F(1,3)(2,6)$ and $F(1,1)(2,4)$, at incident angles of $\theta_i = 54.8^\circ$ and $\theta_i = 57.2^\circ$, respectively. An expansion of this angular range is shown in Fig. 6 for comparison purposes. Both of these features arise from the shadow cone of the first-layer Ni atom interacting with a second-layer Ni atom. One of these features was observed in the clean surface spectrum and is assigned to an $F(1,1)(2,4)$ mechanism. The other feature emerges during oxygen chemisorption. This indicates that, under the assumption that there are no lateral displacements in the surface atoms, there are two values for the spacing between the first and second atomic layer. The first substrate layer atoms are not buckled since only one feature is observed from the $B(1,1)(3,1)$ mechanism. In this case, there is one atom which is located below an oxygen atom at a spacing of $1.91 \pm 0.06 \text{ \AA}$ and there are three atoms at a spacing of $1.65 \pm 0.06 \text{ \AA}$. The buckling amplitude, is, therefore, $0.26 \pm 0.12 \text{ \AA}$. A value of $1.72 \pm 0.06 \text{ \AA}$ is calculated for the distance between the first Ni layer and the weighted average of the two spacings between the first- and second-layer atoms. Considering the value of $3.42 \pm 0.10 \text{ \AA}$ for the spacing between the first and the third layers, the distance between the weighted average position of the second-layer atoms and the third layer is $1.70 \pm 0.16 \text{ \AA}$. These distances are designated as d_{12} and d_{23} in Fig. 7.

Since all the features due to the ion-beam/oxygen interactions are overlapped with intensity features from the

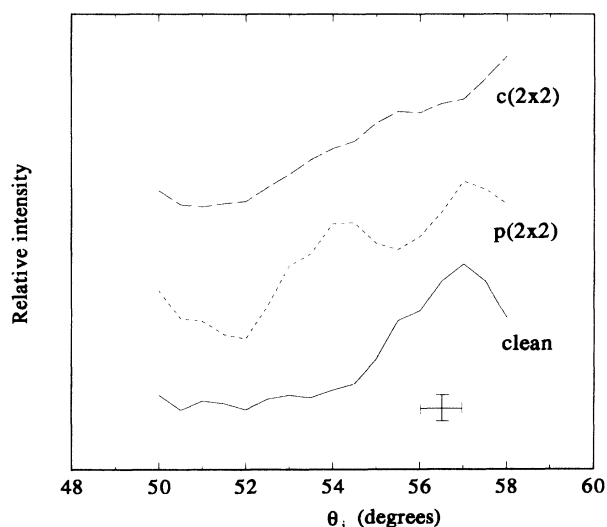


FIG. 6. Expanded region of the data in Fig. 4 between $\theta_i = 50^\circ$ and 58° for clean Ni{001}, $p(2 \times 2)$ O/Ni{001}, and $c(2 \times 2)$ O/Ni{001}. Included in the lower right-hand corner are the associated error bars for all of the data presented.

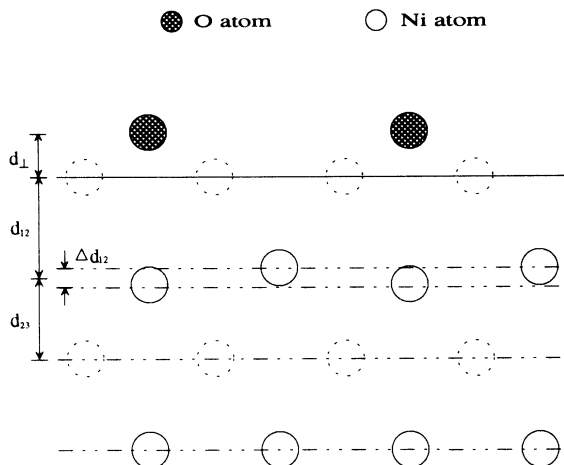


FIG. 7. Cross section of the O/Ni{001} system to illustrate the buckling effect and to define the distances reported in Table II. The distance d_{12} is determined from the weighted average of the two first-to-second-layer spacings. The distance d_{23} is determined from d_{12} .

substrate, it is difficult to speculate about the quantitative nature of the oxygen overlayer structure from this spectrum alone. The feature $F(\text{Ox})(2,6)$ appearing at $\theta_i = 49.8^\circ$ in the $\langle 110 \rangle$ azimuth (Fig. 5) may be used to determine the height of the oxygen overlayer above the Ni surface. This feature results from the shadow-cone edge of the oxygen atom impinging on the Ni atom in the second substrate layer. In order to calculate the O-Ni distance, the shape of the Ar^+/O shadow cone was computed using a Firsov screening factor of 0.86.²⁸ Based on this shadow-cone shape, the distance between the oxygen atom and the Ni atom directly below is $2.76 \pm 0.05 \text{ \AA}$. Combined with the value of $1.91 \pm 0.06 \text{ \AA}$, determined as the distance between the top Ni layer and the second-layer atom directly below an oxygen atom, the height of the oxygen overlayer above the Ni substrate is determined to be $0.85 \pm 0.11 \text{ \AA}$, equivalent to a first-layer-Ni-to-oxygen bond length of 1.96 \AA . The shadow-cone interactions of the oxygen overlayer with the Ni substrate, including the interactions in the $\langle 100 \rangle$ azimuth, have been calculated and are illustrated in Figs. 4 and 5.

C. $c(2 \times 2)$ O/Ni{001}

The distributions of the secondary Ni^+ -ion intensity for the $\langle 100 \rangle$ and $\langle 110 \rangle$ azimuths of the $c(2 \times 2)$ O/Ni{001} surface are plotted in Figs. 4 and 5, respectively. Both spectra exhibit the dominant feature $B(1,1)(1,3)$ at $\theta_i = 22.2^\circ$, as observed in the spectra of the clean and $p(2 \times 2)$ surfaces. From this feature, a value of $3.49 \pm 0.06 \text{ \AA}$ is calculated for the distance between the first and third Ni layers. This may represent a slight expansion compared to the clean and $p(2 \times 2)$ surfaces where we reported a value of $3.42 \pm 0.10 \text{ \AA}$. The magnitude of the uncertainty, however, makes this conclusion quite tentative. The distance between an overlayer oxygen atom and a second-layer Ni atom directly below is determined from the same feature as the one utilized in the $p(2 \times 2)$ analysis, specifically, $F(\text{Ox})(2,6)$ in the $\langle 110 \rangle$ azimuth at $\theta_i = 48.9^\circ$. The distance of $2.83 \pm 0.06 \text{ \AA}$ is larger than the value obtained for the $p(2 \times 2)$ structure. The difference is attributed to the inward displacement of second-layer atoms of the $c(2 \times 2)$ surface, which has also been reported in RBS (Refs. 16 and 17) and LEED (Refs. 18, 19, and 34) studies. The shoulder feature $F(1,1)(2,4)$ at $\theta_i = 55.9^\circ$ in the $\langle 100 \rangle$ azimuth yields an almost bulk-like spacing of $1.78 \pm 0.06 \text{ \AA}$ as the distance from the first Ni layer to the Ni atom located directly below a site that does not contain an oxygen atom.

The feature $F(1,3)(2,6)$ observed in the $p(2 \times 2)$ experiment is no longer resolved in this spectrum and we are unable to directly determine the amplitude of the second-layer buckling from this mechanism. However, the distance from the oxygen atom to the second-layer Ni atom is 2.83 \AA as determined by $F(\text{Ox})(2,6)$. If we assume that the distance between the oxygen atom and the surface Ni plane is 0.85 \AA , the same as that found for the $p(2 \times 2)$ structure, then the distance between the surface Ni plane and the corresponding second-layer Ni atom is $1.98 \pm 0.15 \text{ \AA}$. This value yields a buckling amplitude Δd_{12} of $0.20 \pm 0.12 \text{ \AA}$ for the $c(2 \times 2)$ structure. Moreover, $d_{12} = 1.88 \pm 0.06 \text{ \AA}$ and $d_{23} = 1.61 \pm 0.16 \text{ \AA}$. The final results of our analysis are summarized in Table II, with the distance definitions given in Fig. 7.

We have assumed that the Ni-O bond length is the same for the $c(2 \times 2)$ and the $p(2 \times 2)$ surfaces. Although this assumption is commonly accepted, results from a re-

TABLE II. Shadow-cone-enhanced SIMS analysis of Ni{001}, $p(2 \times 2)$ O/Ni{001}, and $c(2 \times 2)$ O/Ni{001} with comparison to previous studies.

	d_1 (Å) ^a	d_{12} (Å)	d_{23} (Å)	Δd_{12} (Å)	Technique	T (K)	Ref.
Clean		1.70 ± 0.01			RBS	370	17
		1.68 ± 0.06	1.74 ± 0.16		SIMS	300	present work
$p(2 \times 2)$	0.86 ± 0.10	1.80 ± 0.02			RBS	370	17
	0.80 ± 0.05	1.80 ± 0.02	1.75 ± 0.02	0.10 ± 0.07	LEED	120	19
	0.85 ± 0.11	1.72 ± 0.06	1.70 ± 0.16	0.26 ± 0.12	SIMS	300	present work
$c(2 \times 2)$	0.86 ± 0.10	1.85 ± 0.03			RBS	370	17
	0.77 ± 0.04	1.87 ± 0.02		0.035 ± 0.02	LEED	120	18
	0.85 ± 0.11	1.88 ± 0.06	1.61 ± 0.16	0.20 ± 0.10	SIMS	300	present work

^aSee Fig. 7 for definition of distances.

cent x-ray photoelectron spectroscopy (XPS) study³⁵ suggest that the oxygen atom is only 0.3 Å above the surface plane, a value also consistent with a theoretical prediction.³⁶ If we use this value to calculate the buckling magnitude as noted above, we obtain a value of 0.75 Å for Δd_{12} . This very large value is outside the range of physically reasonable values for this system.

Our results reveal that there is a contraction of the second substrate interlayer spacing of 0.06 and 0.15 Å for $p(2 \times 2)$ and $c(2 \times 2)$, respectively. Considering the strong relaxation and reconstruction of the substrate surface, it is possible that even deeper layers could experience atomic displacement. Unfortunately, measurement of this effect is beyond the capabilities of this technique.

For the $c(2 \times 2)$ structure, the second substrate layer buckling amplitude is determined as 0.2 Å, a value which is slightly smaller than the value determined for the $p(2 \times 2)$ buckling (0.26 Å). A local chemical effect argument has been introduced to explain the buckling of the substrate after oxygen adsorption.¹⁹ The Ni atoms beneath oxygen overlayer atoms are relaxed inward in order to reduce the energy of the oxygen adsorbed in the fourfold hollow site. The Ni atoms, which are not beneath oxygen atoms, do not experience the same magnitude of change in the local environment so the atoms are buckled. For the $c(2 \times 2)$ surface, the buckling of the Ni atoms decreases slightly because the added 0.25 monolayer of oxygen reduces the local nature of the chemical effect. The oxygen-induced expansion of the top substrate spacing has been explained as the result of substantial softening of surface force constants, which results in a shift of the surface phonon frequencies.^{37,38}

IV. CONCLUSION AND PROSPECTS

Buckling of second-layer atoms associated with chemisorption has now been observed in many different systems. So far, results from these observations have not allowed a general theory of this phenomenon to be developed. For example, for (2×2) S/Cu{001} the second-layer Cu atom is relaxed toward the surface by 0.13 Å by a S atom bound in the fourfold hollow site directly above it.³⁹ For the very similar $c(2 \times 2)$ S/Ni{001} system, one study reports the second-layer Ni atom is also relaxed toward the surface but only by 0.03 Å,⁴⁰ although another finds that this distance is expanded

by 0.01 Å.⁴¹ For $c(2 \times 2)$ Cl/Cu{001}, $c(2 \times 2)$ S/Ni{011}, and $p(2 \times 2)$ ethylidyne/Pt{111}, the second-layer metal atoms are all relaxed away from the surface plane by 0.04,⁴² 0.1,⁴³ and 0.08 Å,⁴⁴ respectively. Interestingly, for the (2×2) ethylidyne/Rh{111} system, this layer spacing changes in the opposite direction, with the spacing contracting by 0.1 Å.⁴⁵ Obviously, more effort is required before a coherent picture of this effect emerges.

In this study we demonstrate that shadow-cone-enhanced SIMS is applicable to the investigation of adsorbate binding as well as substrate structure. The shadowing effect makes this technique very surface specific, providing information about the top layer that is well resolved from the bulk. Moreover, the nature of the secondary-ion desorption enables this technique to reveal structural information in the second or even deeper layer of the substrate. These types of direct approaches offer complementary approaches to diffraction techniques where structures are selected from a set of candidate structures by comparison between calculation and experiment after transformation from reciprocal-lattice space.

We believe that in the future shadow-cone-enhanced SIMS can make a significant contribution towards examining systems of the type reported here, particularly because of its experimental simplicity. Further improvement of the precision of the technique should be possible by incorporating substrate cooling during data acquisition. Many commonly studied elements have bulk rms thermal vibration amplitudes between 0.05 and 1.0 Å,⁴⁶ and this value may be even higher for surface atoms.⁴⁷ Preliminary investigations show that this factor is largely responsible for the wide peak width (approximately 5° width at half maximum) of an enhanced intensity feature at a substrate temperature of 300 K and that the width could be substantially reduced by cooling to 100 K.⁴⁸

ACKNOWLEDGMENTS

The authors appreciate many helpful discussions with R. Braun, J. O'Connor, and D. A. Shirley. This work was partially supported by funds from the National Science Foundation, the Office of Naval Research, and the Department of Energy. One of us (C.X.) wishes to thank Dr. K. David for providing the Ni crystal.

¹S. Andersson, B. Kasemo, J. B. Pendry, and M. A. Van Hove, *Phys. Rev. Lett.* **31**, 595 (1973).

²J. E. Demuth and T. N. Rhodin, *Surf. Sci.* **45**, 249 (1974).

³P. M. Marcus, J. E. Demuth, and D. W. Jepsen, *Surf. Sci.* **53**, 501 (1975).

⁴G. Hanke, E. Lang, K. Heinz, and K. Müller, *Surf. Sci.* **91**, 551 (1980).

⁵S. Y. Tong and K. H. Lau, *Phys. Rev. B* **25**, 7382 (1982).

⁶J. E. Demuth, N. J. DiNardo, and G. S. Cargill III, *Phys. Rev. Lett.* **50**, 1373 (1983).

⁷S. R. Chubb, P. M. Marcus, K. Heinz, and K. Müller, *Phys.*

Rev. B **41**, 5417 (1990).

⁸J. Stöhr, R. Jaeger, and T. Kendelewicz, *Phys. Rev. Lett.* **49**, 142 (1982).

⁹L. Wenzel, D. Arvanitis, W. Daum, H. H. Rotermund, J. Stöhr, K. Baberschke, and H. Ibach, *Phys. Rev. B* **36**, 7689 (1987).

¹⁰K. H. Rieder, *Phys. Rev. B* **27**, 6978 (1983); *Surf. Sci.* **128**, 325 (1983).

¹¹R. W. Godby and N. Garcia, *Surf. Sci.* **163**, L681 (1985).

¹²G. Allan and J. Lopez, *Surf. Sci.* **95**, 214 (1980).

¹³T. S. Rahman, J. E. Black, and D. L. Mills, *Phys. Rev. Lett.*

- 46, 1469 (1981).
- ¹⁴S. Masuda, M. Nishijima, Y. Sakisaka, and M. Onchi, *Phys. Rev. B* **25**, 863 (1982).
- ¹⁵S. Andersson, P.-A. Karlsson, and M. Persson, *Phys. Rev. Lett.* **51**, 2378 (1983).
- ¹⁶J. W. M. Frenken, J. F. van der Veen, and G. Allen, *Phys. Rev. Lett.* **51**, 1876 (1983).
- ¹⁷J. W. M. Frenken, R. G. Smeenk, and J. F. van der Veen, *Surf. Sci.* **135**, 147 (1983).
- ¹⁸W. Oed, H. Lindner, U. Starke, K. Heinz, K. Müller, and J. B. Pendry, *Surf. Sci.* **224**, 179 (1989).
- ¹⁹W. Oed, H. Lindner, U. Starke, K. Heinz, K. Müller, D. K. Saldin, P. de Andres, and J. B. Pendry, *Surf. Sci.* **225**, 242 (1990).
- ²⁰A. G. J. de Wit, R. P. N. Bronckers, and J. M. Fluit, *Surf. Sci.* **82**, 177 (1979).
- ²¹C. C. Chang and N. Winograd, *Phys. Rev. B* **39**, 3467 (1989).
- ²²C. Xu, K. P. Caffey, J. S. Burnham, S. H. Goss, B. J. Garrison, and N. Winograd, *Phys. Rev. B* **45**, 6776 (1992).
- ²³C. C. Chang and N. Winograd, *Surf. Sci.* **230**, 27 (1990).
- ²⁴R. Smith, D. E. Harrison, Jr., and B. J. Garrison, *Phys. Rev. B* **40**, 93 (1989).
- ²⁵R. Blumenthal, S. K. Donner, J. L. Herman, R. Trehan, K. P. Caffey, E. Furman, N. Winograd, and B. D. Weaver, *J. Vac. Sci. Technol. B* **6**, 1444 (1988).
- ²⁶K. P. Caffey, R. Blumenthal, J. Burnham, E. Furman, and N. Winograd, *J. Vac. Sci. Technol. B* **9**, 2268 (1991).
- ²⁷R. Blumenthal, K. P. Caffey, E. Furman, B. J. Garrison, and N. Winograd, *Phys. Rev. B* **44**, 12 830 (1991).
- ²⁸D. J. O'Connor and R. J. MacDonald, *Radiat. Eff.* **34**, 247 (1977).
- ²⁹D. W. Jepsen, P. M. Marcus, and F. Jona, *Phys. Rev. B* **5**, 3933 (1972).
- ³⁰H. L. Davis and J. R. Noonan, *Surf. Sci.* **126**, 245 (1983).
- ³¹J. W. M. Frenken, J. F. van der Veen, R. N. Barnett, U. Landman, and C. L. Cleveland, *Surf. Sci.* **172**, 319 (1986).
- ³²J. E. Demuth, P. M. Marcus, and D. W. Jepsen, *Phys. Rev. B* **11**, 1460 (1975).
- ³³P. R. Watson, F. R. Shepherd, D. C. Frost, and K. A. R. Mitchell, *Surf. Sci.* **72**, 562 (1978).
- ³⁴J. H. Onuferko, D. P. Woodruff, and B. W. Holland, *Surf. Sci.* **87**, 357 (1979).
- ³⁵E. Kopatzki and R. J. Behm, *Surf. Sci.* **245**, 255 (1991).
- ³⁶T. H. Upton and W. A. Goddard III, *Phys. Rev. Lett.* **46**, 1635 (1981).
- ³⁷T. S. Rahman, D. L. Mills, J. E. Black, J. M. Szeftel, S. Lehwald, and H. Ibach, *Phys. Rev. B* **30**, 589 (1984).
- ³⁸T. S. Rahman and H. Ibach, *Phys. Rev. Lett.* **54**, 1933 (1985).
- ³⁹C. C. Bahr, J. J. Barton, Z. Hussain, S. W. Robey, J. G. Tobin, and D. A. Shirley, *Phys. Rev. B* **35**, 3773 (1987).
- ⁴⁰J. J. Barton, C. C. Bahr, S. W. Robey, Z. Hussain, E. Umbach, and D. A. Shirley, *Phys. Rev. B* **34**, 3807 (1986).
- ⁴¹W. Oed, U. Starke, K. Heinz, K. Müller, and J. B. Pendry, *Surf. Sci.* **251/252**, 488 (1991).
- ⁴²Li-Qiong Wang, A. E. Schach von Wittenau, Z. G. Ji, L. S. Wang, Z. Q. Huang, and D. A. Shirley, *Phys. Rev. B* **44**, 1292 (1991).
- ⁴³S. W. Robey, J. J. Barton, C. C. Bohr, G. Liu, and D. A. Shirley, *Phys. Rev. B* **35**, 1108 (1987).
- ⁴⁴U. Starke, A. Barbieri, N. Materer, M. A. Van Hove, and G. A. Somorjai, *Surf. Sci.* **286**, 1 (1993).
- ⁴⁵A. Wander, M. A. Van Hove, and G. A. Somorjai, *Phys. Rev. Lett.* **67**, 626 (1991).
- ⁴⁶D. S. Gemmell, *Rev. Mod. Phys.* **46**, 129 (1974).
- ⁴⁷A. U. Macrae, *Surf. Sci.* **2**, 522 (1964).
- ⁴⁸C. Xu, J. S. Burnham, and N. Winograd (unpublished).